Chinese Journal of Catalysis 52 (2023) 176–186

available at www.sciencedirect.com

ScienceDirect

journal homepage: www.sciencedirect.com/journal/chinese-journal-of-catalysis

Article

Bidirectional host-guest interactions promote selective photocatalytic CO_2 reduction coupled with alcohol oxidation in aqueous solution

Wen Zhang [a,1], Cai-Cai Song [a,1], Jia-Wei Wang [b], Shu-Ting Cai [a], Meng-Yu Gao [a], You-Xiang Feng [a], Tong-Bu Lu [a,*]

[a] *MOE International Joint Laboratory of Materials Microstructure, Institute for New Energy Materials and Low Carbon Technologies, School of Materials Science and Engineering, Tianjin Key Laboratory of Organic Solar Cells and Photochemical Conversion, School of Chemistry and Chemical Engineering, Tianjin University of Technology, Tianjin 300384, China*

[b] *KLGHEI of Environment and Energy Chemistry, School of Chemistry, Sun Yat-sen University, Guangzhou 510275, Guangdong, China*

ARTICLE INFO

Article history:
Received 17 May 2023
Accepted 13 August 2023
Available online 25 September 2023

Keywords:
Artificial photosynthesis
Host-guest interaction
CO_2 reduction
Alcohol oxidation
Fast electron transfer

ABSTRACT

Existing artificial photosynthesis systems often underperform due to challenges in water oxidation and extensive photogenerated carrier transfer. Herein, we demonstrate that *β*-cyclodextrin-decorated CdS nanocrystals (CdS-CD) can simultaneously anchor cobalt tetraphenyl porphyrin (CoTPP) catalysts and alcohol reductants onto CdS surfaces through bidirectional host-guest interactions between *β*-CD and CoTPP/alcohol. This configuration ensures swift electron transfer from CdS to *β*-CD bonded CoTPP, facilitating CO_2 reduction to HCOOH. Results showcase a remarkable yield of 1610 μmol g^{-1} h^{-1} and a 96.5% selectivity. Meanwhile, photogenerated holes in CdS are efficiently neutralized by *β*-CD bonded furfuryl alcohol, achieving a furfural yield of 1567 μmol g^{-1} h^{-1} and > 99% selectivity. In contrast, the discrete CoTPP-CdS system achieved a HCOOH yield of only 306 μmol g^{-1} h^{-1} and a poor HCOOH selectivity of 46.4%. It was also observed that the CoTPP@CdS-CD system maintained high CO_2-to-HCOOH conversion rates when using other alcohols as reductants.

1. Introduction

Constructing efficient artificial photosynthesis systems to convert CO_2 into diverse chemicals offers a sustainable solution to counter global warming and the current energy crisis [1–5]. To bring artificial photosynthetic technologies toward practical applications, a carbon cycle of CO_2 reduction coupled with H_2O oxidation is considered an ideal approach to convert solar energy into chemical energy [6,7], mirroring natural photosynthesis. To date, various semiconductors such as TiO_2 [8–10], $CsPbBr_3$ [11,12], Cu_2O [13,14], and BiOBr [15], have been developed as photocatalysts for this coupled process. However, the significant kinetic barrier in the water oxidation reaction hinders optimal photocatalytic CO_2 reduction. Therefore, additional electron sacrificial agents, such as triethanolamine (TEOA) [16–18], triethyl amine (TEA) [19–21], and 1,3-dimethyl-2-phenyl-2,3-dihydro-1H-benzo[d]imidazole (BIH) [22,23], have been employed as electron donors to en-

* Corresponding author. E-mail: lutongbu@tjut.edu.cn (T.-B. Lu).
This work was supported by the National Natural Science Foundation of China (21702146, 21790052, 21931007), the National Key R&D Program of China (2022YFA1502902), 111 Project of China (D17003), and the Natural Science Foundation of Tianjin (19JCQNJC05500).
[1] Contributed equally to this work.
https://doi.org/10.1016/S1872-2067(23)64509-7

hance CO_2 photocatalytic reduction. Yet, using these agents is economically unfeasible and also underutilizes the oxidation potential of the photogenerated holes. Consequently, pairing the CO_2 reduction with organic oxidation to produce value-added chemicals has emerged as a viable approach for real-world application [24–30]. Moreover, if the organics are derived from biomass, only renewable resources are consumed [31].

In aqueous systems, the CO_2 reduction selectivity often faces challenges due to competitive hydrogen evolution, necessitating an additional CO_2 reduction catalyst to work in tandem with semiconductors to boost CO_2 reduction selectivity. For a combined CO_2 reduction and organic oxidation in a single photocatalytic system, the synchronized consumption of photogenerated electrons and holes is vital, as it can minimize carrier recombination [32–34]. In a discrete photocatalytic system, compromising a photosensitizer, catalyst, and reactant (Scheme 1(a)), the electron transfer efficiency hinges on the diffusion process from the photosensitizer to the catalyst. This diffusion is constrained by an upper rate constant limit of ~10^{10} L mol^{-1} s^{-1} [35]. Aiming to amplify electron transfer efficiency, certain researchers have attempted to shorten the gap between the catalyst and photosensitizer by building a "bridge" between them (Scheme 1(a)). For example, Sun and Ishitani have constructed a series of supramolecular photocatalytic systems by linking Re-/Ru-based catalysts with various photosensitizers using covalent bridging ligands [36–38]. Compared with discrete systems, these supramolecular systems showcased faster intramolecular electron transfer rates (~1.4×10^9 s^{-1}) and enhanced CO_2 reduction efficacy [37]. Yet, the creation of such diad systems demands intricate synthesis, relies on valuable metal-based catalysts, and there is a risk of covalent bond disruptions during electron transport, potentially compromising system stability and efficiency [39].

Compared with covalent bonding, connecting the photosensitizer and catalyst through noncovalent interactions, such as hydrogen bonding and electrostatic interactions, is more synthetically accessible. Moreover, these dynamic, reversible interactions potentially enhance the endurance and stability of the photocatalytic performance (Scheme 1(a)). To this end, unidirectional noncovalent strategies leveraging electrostatic interactions [16,40], and hydrogen bonds [41,42] have been investigated to merge the photosensitizer and catalyst, thereby optimizing electron transfer for CO_2 reduction. Yet, these systems' efficiency is often compromised by a sluggish hole elimination rate due to the extended hole transfer distance between the photosensitizer and reactant.

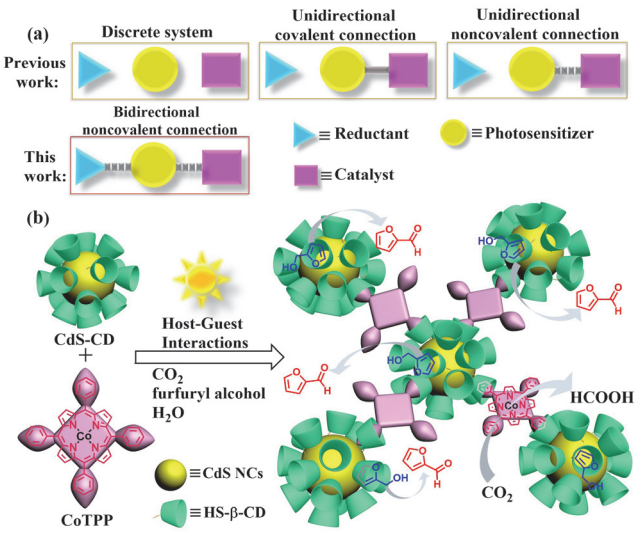

Scheme 1. (a) Four different connection modes between reductant, photosensitizer, and catalyst in a photocatalytic system. (b) Self-assembly of CdS-CD NCs with CoTPP through host-guest interactions and their photoredox reactions of CO_2 to HCOOH and furfuryl alcohol to furfural.

Herein, we introduce a highly efficient photocatalytic system devised through bidirectional host–guest interaction, in which the water-soluble mono-(6-mercapto-6-deoxy)-*β*-cyclodextrin-decorated CdS nanocrystals (CdS-CD NCs) can concurrently gather the cobalt meso-tetraphenylporphyrin (CoTPP) catalyst and furfuryl alcohol organic reactant on the surface of the CdS NCs. This assembly is facilitated by host-guest interactions between *β*-CD and CoTPP/alcohols (Scheme 1(b)). The immediate association of CdS NCs with both CoTPP and alcohols, combined with the straightforward oxidation of alcohols, is expected to result in swift consumption of the photogenerated carriers. Consequently, the CO_2 reduction reaction efficiency is poised to surpass that of the discrete CoTPP-CdS photocatalytic system.

2. Experimental

2.1. Materials

Mono-(6-mercapto-6-deoxy)-*β*-cyclodextrin (HS-*β*-CD) was purchased from Zhiyuan Biotchnology, and used without further purification. Sulfur (powder, 99%), 1-octadecene (ODE, 90%), cadmium oxide (CdO, 99%), and tetrabutylammonium hexafluorophosphate (TBAPF6, 98%) were purchased from Aladdin. Trimethyloxonium tetrafluoroborate ($C_3H_9OBF_4$, AR, 98%) was purchased from Heowns. Oleic acid (OA, 90%) and tetramethylammonium hydroxide pentahydrate (TMAOH, 97%), *n*-hexane (HPLC, 95%) were purchased from Adamas. Methanol (AR, 99.5%) was purchased from J&K. Acetone (AR, 99.5%) and trichloromethane (AR, 99%) was purchased from Sinopharm Chemical Reagent Co., Ltd. $^{13}CO_2$ was purchased from Sigma. All the other chemicals are commercially available and used without further purification. The photocatalytic experiments were carried out in pure water under carbon dioxide atmosphere.

2.2. Preparation

Oleic acid (OA) capped CdS NCs (CdS-OA) were prepared according to a reported procedure. Firstly, cadmium oxide (640 mg, 4.21 mmol), 1-octadecene (88 mL) and oleic acid (29 mL) were added sequentially to a 1000 mL three-mouth flask. The mixture was heated to 285 °C under Ar atmosphere. Then, a solution of sulfur (0.08 g, 2.5 mmol) in 1-octadecene (38 mL) was added rapidly and reacted for 120 s before rapidly cooled

to 25 °C by an ice bath. The reaction mixture was added to the methanol/*n*-hexane (*V*:*V* = 1:1, 200 mL) solvent, followed by excessive acetone to produce precipitation. The precipitate was centrifuged at 7000 r min^{-1} for 3 min, and washed with n-hexane and acetone for 3 times. The obtained CdS-OA was dissolved in *n*-hexane for further use.

HS-*β*-CD (83.5 mg) was firstly dispersed in a mixture solution of water (4 mL), methanol (5 mL) and chloroform (5 mL), and the pH value of the solution was adjusted to 12 by tetramethylammonium hydroxide pentahydrate. Then, the hexane solution of CdS-OA (0.016 μmol) was added to the above solution, and stirred in the dark for two days. After that, the generated CdS-CD was precipitated by excess acetone and centrifuged (7000 r min^{-1}) for 3 min. Finally, the crude CdS-CD was washed with acetone before being dispersed in water (1 mL).

CdS-ME was prepared by a procedure similar to that of CdS-CD, expect using 2-mercaptoethanol to instead of HS-*β*-CD.

The ligand stripping reaction was carried out with a modified literature method. Firstly, the solvent of the *n*-hexane solution of CdS-OA (2 mL) was removed by rotary evaporation. The obtained solid was dissolved in a mixture solution of $CHCl_3$/DMF (*V*:*V* = 15:1, 6.4 mL), and a acetonitrile solution of trimethyloxonium tetrafluoroborate was added into the mixture until particles were precipitated. Then, the reaction solution was stirred for 10 min, and centrifuged (7000 r min^{-1}) for 3 min. After being dried in air for 1 min, CdS-BF_4 was redispersed in DMF (2 mL) for further use.

2.3. Characterization

Ultraviolet-visible (UV-vis) absorption spectra were recorded with a Lambda 750 UV-vis spectrophotometer. Fourier transform infrared spectroscopy (FTIR) spectra were recorded on a Frontier Mid-IR FTIR. Power X-ray diffraction (XRD) measurements were carried out on a RIGAKU Smart Lab diffractometer, using Cu K_α radiation operated at 9 KW power. Transmission electron microscope (TEM) images were recorded on a Tecnai G2 Spirit TWIN transmission electron microscope (FEI). Nuclear magnetic resonance (NMR) spectra were recorded on a Bruker 400 MHz instrument in D_2O, and chemical shifts were recorded in parts per million (ppm). The steady-state photoluminescence spectra (PL) were measured using F-4600 Fluorescence spectrophotometer (Hitachi) under excitation at 420 nm. Dynamic light scattering (DLS) measurements were examined using a laser-light scattering spectrometer equipped with a digital correlator of 636 nm under a scattering angle of 90° (Brookhaven). The time-resolved fluorescence measurements were detected with a time-resolved confocal fluorescence microscopic imager (Microtime 200, PicoQuent, Germany, Table S1, Entries 1–8), well as a FLS-1000 steady state and transient state fluorescence spectrometer (Edinburgh Instruments Ltd., Table S1, Entries 9–11), with excitation wavelength at 450 nm and detection wavelength at 660 nm. X-ray photoelectron spectroscopy (XPS) patterns were detected by an ESCALAB 250Xi X-ray photoelectron spectrometer, with Al K_α as the excitation source (Thermo scientific). Liquid products after reaction were identified by high performance liquid chromatogram (HPLC, Shimadzu, Japan) and ion chromatography (IC, Eco IC, Metrohm). The products in gas phase were analyzed in a GC-2014 gas chromatograph instrument (GC, SHIMADZU) equipped with TCD and FID dual detectors.

Electron paramagnetic resonance (EPR) was measured on a Bruker EPR spectrometer (Bruker, EMXplus-6/1, Germany). An aqueous solution (0.5 mL) of CdS-CD (1 μmol L^{-1}) and furfuryl alcohol (0.3 mol L^{-1}) was added to a DMSO solution of CoTPP (5 μM, 0.5 μL) and DMPO (5,5-dimethyl-1-pyrroline-N-oxide, 1 mol L^{-1}) in a quartz tube. After saturated with CO_2, the reaction system was continuously stirred and illuminated by a 300-W Xe lamp at room temperature. The EPR measurement was started after 15 min of illumination with the following measuring conditions: centerfield 3515 G; sweep width 200 G; microwave power 2 mW; modulation frequency 100 kHz; modulation amplitude 1.0 G; conversion time 30 ms; sweep time 60 s.

2.4. Photoelectrochemical experiments

All the electrochemical characterizations were performed on the CHI760E electrochemical workstation with a three-electrode system. Catalyst coated FTO glass (1 cm^2), Pt sheet and Ag/AgCl (in 3 mol L^{-1} KCl) were employed as the working electrode, counter electrode, and reference electrode, respectively. Before the measurement, high purity CO_2 was injected in the electrolyte for 40 min. The electrochemical impedance spectroscopy (EIS) measurements were conducted under xenon lamp irradiation, and the AC voltage amplitude of 5 mV was set with frequency range from 0.01 to 10^6 Hz. The corresponding Nyquist spectra was fitted with ZView 2. The photo-response of the prepared photoelectrodes (*I*-*t*) was evaluated by recording the photocurrent density at a bias potential of −0.4 V (*vs.* Ag/AgCl) under the same irradiation conditions.

2.5. Photocatalytic CO_2 reduction and alcohol oxidation

Typically, an aqueous solution of CdS-CD (1 μmol L^{-1}), furfuryl alcohol/cinnamic alcohol (0.3 mol L^{-1}), the DMSO solution of CoTPP (5 μmol L^{-1}, 1 μL), and water (1 mL) were added into a quartz tube. After saturated with CO_2, the reaction system was continuously stirred and illuminated by a 300-W Xe lamp with 420 nm light filter for 1 h at room temperature. The species and selectivity of the products in gas and liquid phase were determined by GC, IC and HPLC measurements, respectively.

3. Results and discussion

3.1. Synthesis and characterization.

We first employed cyclic voltammetry (CV) to ascertain the redox potentials of CoTPP and furfuryl alcohol in a 0.5 mol L^{-1} $KHCO_3$ electrolyte. This was done using an Au electrode covered with –S-*β*-CD that binds the CoTPP catalyst (refer to Supporting Information), Ag/AgCl, and Pt foil as the working, ref-

erence, and counter electrodes, respectively. As illustrated in Fig. 1(a), with the introduction of CO_2, CoTPP shows an enhanced current at a potential of −0.75 V *vs.* NHE (i.e., the onset potential). This suggests that a monoelectronic redox species of $[Co^{I}TPP]^{-}$ might be the operative entity for CO_2 reduction. In contrast, in a homogeneous DMF system, CO_2 reduction takes place on the second electron reduction species of $[Co^{0}TPP]^{2-}$ using a glass carbon working electrode (Fig. 1(a), inset). This observation aligns with prior findings: when CoTPP is immobilized in a nanostructure, $[Co^{I}TPP]^{-}$ demonstrates heightened catalytic activity toward CO_2 reduction in water [43,44]. Furthermore, the oxidation potential of furfuryl alcohol was identified to be 1.03 V *vs.* NHE (Fig. 1(b)).

Following this, we synthesized CdS-CD NCs in line with our previous research [45]. The detailed synthesis steps and characterizations, encompassing power XRD, FTIR, and TEM (Figs. S1–S4). To determine the band structure of CdS-CD, we undertook UV-vis absorption spectroscopy and Mott-Schottky plot analysis. Notably, the UV-vis absorption spectrum of CdS-CD closely mirrored that of the initial CdS-OA (where OA = oleic acid, as shown in Fig. S5), suggesting the ligand exchange process retained the inherent band structure of CdS NCs. By converting the plot of $(\alpha h\nu)^2$ in relation to photon energy, the band gap of CdS-CD was approximated at 2.59 eV (Fig. 1(c), inset). Additionally, the conduction band (CB) of CdS-CD was gauged at −0.97 V *vs.* NHE, as derived from the Mott-Schottky plot (Fig. 1(c)). Subsequently, the energy-band position of CdS-CD, combined with the redox attributes of CoTPP and furfuryl alcohol, was illustrated in Fig. 1(d). As our results indicate, under visible light exposure, CdS-CD's photogenerated electrons transition from its CB to the cobalt center of $Co^{II}TPP$. This initiates a one-electron reduction, leading to the formation of $[Co^{I}TPP]^{-}$, which subsequently binds to and reduces CO_2. Meanwhile, the photogenerated holes on the VB of CdS-CD are also energetically competent in the oxidation of furfuryl alcohol.

3.2. Host-guest interactions among CdS-CD, CoTPP, and furfuryl alcohol

The hydrophilic exterior and hydrophobic cavity of *β*-CD grant it the distinctive ability to envelop hydrophobic groups of suitable sizes through host-guest interactions, reminiscent of enzyme-substrate recognition in the natural world [46–48]. Initially, we studied these interactions between *β*-CD and CoTPP. The comparative ^{1}H NMR spectra (Fig. S6) showed a high field shift of protons on CoTPP's benzene ring with the introduction of *β*-CD. This implies that *β*-CD's cavity captures the benzene ring of CoTPP [49]. In addition, Job's plot analysis revealed a 2:1 inclusion stoichiometry between *β*-CD and CoTPP (Fig. 2(a), calculated from the data presented in Figs. S7 and S8). Successive binding constants between *β*-CD and CoTPP were established *via* UV-vis absorption titration, resulting in 3.89×10^{4} L mol^{-1} (for the initial *β*-CD equivalent) and 1.59×10^{5} L mol^{-1} (for the second *β*-CD equivalent) (Fig. 2(b)). UV-vis absorption titration also found that binding constants between CdS-bound *β*-CD and CoTPP were 5.59×10^{4} L mol^{-1} and 1.26×10^{5} L mol^{-1}, respectively (Fig. S9). These values align with the *β*-CD and CoTPP interactions, indicating potent host-guest relations between CdS-CD and CoTPP. This allows for a cross-linking of CdS-CD and CoTPP *via* host-guest interactions, leading to an integrated photocatalytic system. This promotes sustained electron injection from CdS-CD to CoTPP, as depicted in Scheme 1 and Fig. 1(d). The formation of a supramolecular assembly of CoTPP@CdS-CD was further confirmed by DLS and

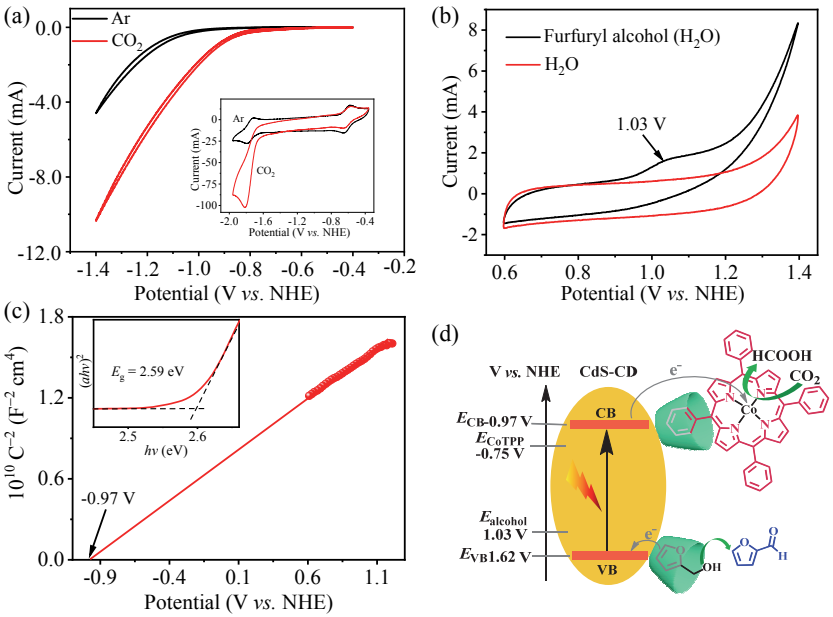

Fig. 1. (a) CV curves for CoTPP bonded on Au electrode covered with −S-*β*-CD in 0.5 mol L^{-1} $KHCO_3$ solution (inset: CoTPP in DMF). (b) CV curves for furfuryl alcohol. (c) Tauc plot $(\alpha h\nu)^2$ *vs.* photon energy (inset) and Mott-Schottky plot of CdS-CD. (d) Band structures of CdS-CD and redox potentials of CoTPP and furfuryl alcohol.

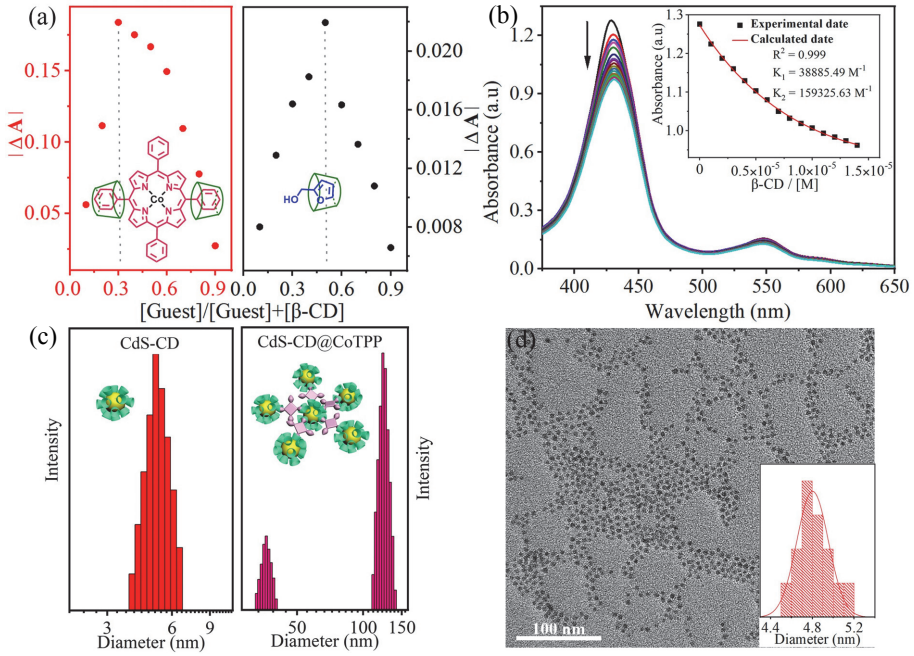

Fig. 2. (a) Job's plot of CoTPP/*β*-CD (red dot) and furfuryl alcohol/*β*-CD (black dot), $\Delta A = A_{(\text{with } \beta\text{-CD})} - A_{(\text{without } \beta\text{-CD})}$, where *A* refers to the absorbance of CoTPP or furfuryl alcohol, and Δ*A* represents the change of the absorbance for CoTPP/furfuryl after adding various proportions of *β*-CD. (b) UV-vis absorption spectra changes for CoTPP upon the addition of *β*-CD in water (inset: the calculated binding constant (K_S) value). (c) DLS measurements of CdS-CD and CoTPP@CdS-CD assembly. (d) TEM image of CoTPP@CdS-CD assembly (inset: size distribution of individual CdS-CDs).

TEM measurements. Contrasting with the singular CdS-CD NCs with a mean size of 4.8 nm (Figs. S3 and 2(c)), CoTPP's addition resulted in pronounced aggregation of CdS-CD NCs (Figs. 2(c) and 2(d)), yielding larger, irregular nanostructures of ~35 and 125 nm in size (Fig. 2(c)), thereby confirming the self-assembly of CdS-CD with CoTPP.

The interaction between *β*-CD and furfuryl alcohol was characterized using ^{1}H NMR spectroscopy, Job's plot analysis, and UV-vis absorption spectroscopy titration experiments. Fig. S10 illustrates that in the presence of *β*-CD, the protons of the furan ring and the methylene group undergo downfield shifts. This indicates that a furfuryl alcohol molecule fits within *β*-CD's cavity. According to the Job's plot (Fig. 2(a), derived from Figs. S11 and S12), the complex ratio of *β*-CD to furfuryl alcohol is approximately 1:1. The binding constant of *β*-CD with furfuryl alcohol, as determined by UV-vis absorption spectroscopy titration, is 465.7 L mol^{-1} (Fig. S13). Consequently, at the outset of the photoreaction, an estimated 95% of *β*-CD on the CdS-CD surface forms complexes with furfuryl alcohol (see Supporting Information for details). These findings suggest that the *β*-CD enveloping the CdS-CD NCs can simultaneously host both CoTPP and furfuryl alcohol through bidirectional host–guest interactions, effectively bringing the catalyst and reactant together on the CdS NCs surface.

3.3. Photocatalytic CO_2 reduction coupled with alcohol oxidation

Motivated by the demonstrated bidirectional host-guest interactions between CdS-CD and CoTPP/furfuryl alcohol, we assessed the photocatalytic performance of the *in-situ* assembled CoTPP@CdS-CD in reducing CO_2 paired with the oxidation of furfuryl alcohol in an aqueous solution, as presented in Table 1 and Fig. 3(a). More specifically, stock solutions of CdS-CD, furfuryl alcohol, CoTPP, and H_2O were sequentially added to a quartz tube reactor. Once saturated with CO_2, the reactor was sealed and illuminated with a 300 W Xe lamp (with a 420 nm filter) at approximately 25 °C. Subsequent analysis of the generated products in both gas and liquid phases was conducted using GC, IC, and HPLC (Figs. S14–S19). As Table 1 (entry 1) indicates, CoTPP@CdS-CD achieved an impressive HCOOH yield of 1609.9 μmol g^{-1} h^{-1}, exhibiting a selectivity of 96.5%. Calculations based on the CoTPP catalyst resulted in turnover number and turnover frequency values of 280 and 280 h^{-1}, respectively (Table S1), with a quantum yield of 0.86% (Table S1, Fig. S20). Meanwhile, furfural yield reached 1567.0 μmol g^{-1} h^{-1} with selectivity exceeding 99%. These metrics outperform most CO_2 reduction coupled alcohol oxidation systems, particularly in aqueous systems (Fig. 3(b), Table S2). Notably, the photoreaction's utilization ratio of photogenerated electrons and holes approached 1, indicating a near-perfect balance between the reduction and oxidation reactions. In sharp contrast, CdS-BF_4 NCs, devoid of surface ligands, only achieved a HCOOH yield of 305.5 μmol g^{-1} h^{-1}, and exhibited an unintended hydrogen evolution side reaction (352.5 μmol g^{-1} h^{-1}, Table 1, entry 2). This observation is attributed to the limited interactions between CdS-BF_4 NCs and CoTPP due to the electrostatic repulsion between them. As a consequence, the photogenerated electrons on the CdS-BF_4 NCs tend to reduce protons in the aqueous solution [50]. Moreover, for oleic acid capped CdS NCs (CdS-OA), the HCOOH yield of 70.1 μmol g^{-1} h^{-1} was notably inferior to CdS-CD's output (Table 1, entry 3). This indicates

Table 1
Comparative experiments for the photocatalytic reduction of CO_2 coupled with furfuryl alcohol oxidation.

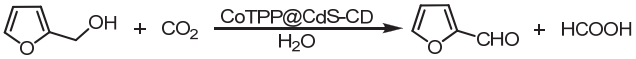

Entry	Ps	H_2 (μmol g^{-1} h^{-1})	HCOOH (μmol g^{-1} h^{-1})	Select. HCOOH (%)	Furfural (μmol g^{-1} h^{-1})	Select. furfural (%)	e^-/h^+
1	CdS-CD	47.0	1609.9	96.5	1567.0	> 99	1.05
2	CdS-BF_4	352.5	305.5	46.4	705.0	> 99	0.93
3	CdS-OA	0	70.1	> 99	68.2	> 99	1.03
4	CdS-ME	523.9	621.6	54.3	605.7 (221.1)	73.2	1.09
5	CdS-BF_4+CD	11.8	481.8	97.6	519.2	> 99	0.95
6 [a]	CdS-CD	37.6	477.2	96.1	474.9	> 99	1.08
7 [b]	CdS-CD	74.5	634.1	89.5	793.2	> 99	0.89

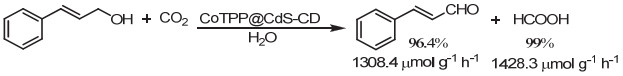

Reaction conditions: CdS-CD (1 μmol L^{-1}), CoTPP (5 μmol L^{-1}), furfuryl alcohol or cinnamic alcohol (0.3 mol L^{-1}), H_2O (1 mL), 300 W Xe lamp (λ > 420 nm, 100 mW cm^{-2}), 1 h, ~25 °C. Entry 4: the value in parentheses is the yield of furoic acid.
[a] With the addition of amantadine hydrochloride.
[b] None CoTPP was employed. Ps: Photosensitizer. Select.: Selectivity.

that the insulating alkyl chains hamper the efficient utilization of photogenerated carriers on the CdS NCs [19]. To further understand the impact of the β-CD ring on the photocatalytic reactions, we synthesized 2-mercaptoethanol-decorated CdS NCs (CdS-ME) for a comparative analysis (Fig. S5). As detailed in Table 1 (entry 4), CdS-ME showcased markedly reduced catalytic activity for HCOOH production (621.6 μmol g^{-1} h^{-1}) when juxtaposed with CdS-CD. Notably, hydrogen evolution was detected alongside furfural (605.7 μmol g^{-1} h^{-1}). Additionally, a significant yield of furoic acid (221.1 μmol g^{-1} h^{-1}, Fig. S19) was observed, attributable to the overoxidation of furfural. This highlights the diminished selectivity of the CdS-ME system for both reduction and oxidation products. Furthermore, a mere physical combination of CdS-BF_4 and native β-CD revealed markedly reduced HCOOH and furfural outputs compared to the CdS-CD system (Table 1, entry 5, Fig. 3(a)). This suggests that the interactions between β-CD and CdS NCs play a pivotal role in determining CdS NCs' catalytic efficiency. Collectively, these findings underscore the importance of β-CD adornment on CdS NCs surfaces in amplifying their photocatalytic prowess.

To determine whether furfuryl alcohol can be completely transformed into furfural with high selectivity, we evaluated the photocatalytic reactions of CoTPP@CdS-CD across different concentrations of furfuryl alcohol. As depicted in Table S3 and Fig. S21, when furfuryl alcohol concentrations decreased from

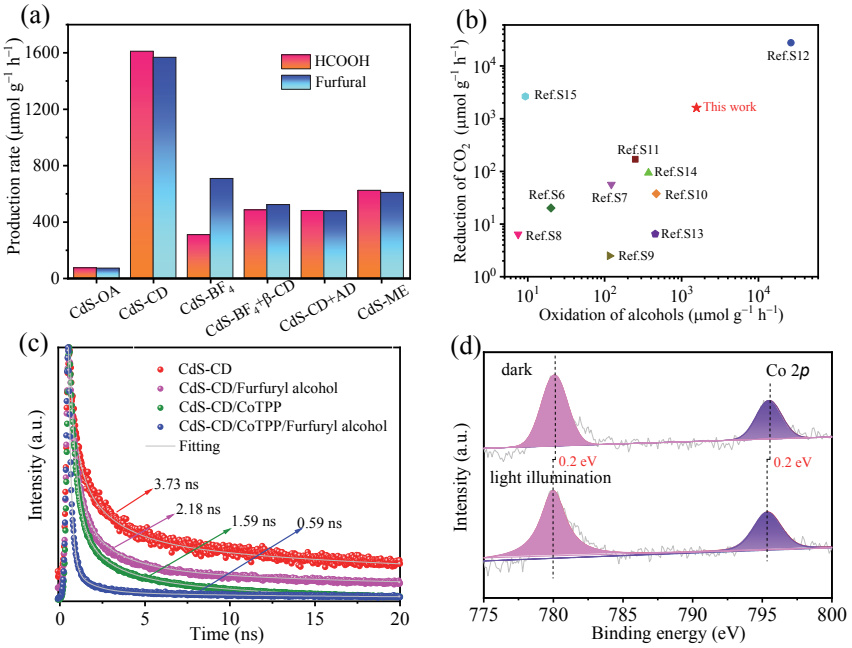

Fig. 3. (a) Production of HCOOH over CdS-OA, CdS-CD, CdS-BF_4, the physical mixture of CdS-BF_4 and β-CD, CdS-CD+AD, and CdS-ME. (b) Comparison of photocatalytic systems coupling the CO_2 reduction with the oxidation of alcohols. (c) Fluorescence decay traces of CdS-CD with furfuryl alcohol and CoTPP. (d) *In-situ* Co 2*p* XPS spectra for the CoTPP@CdS-CD assembly under irradiation by a 300 W Xe lamp equipped with a 420 nm light filter.

25 to 0.6 mmol L^{-1}, the conversion rates of furfuryl alcohol to furfural surged from 3.5% to 97.0%. Impressively, furfural selectivity remained consistently above 99% in all cases, suggesting that furfural did not undergo further oxidation to furoic acid, even at lower furfuryl alcohol concentrations. Notably, there was an absence of O_2 production throughout the photoreaction, as evidenced in Fig. S22. This implies that the CoTPP@CdS-CD catalyst is not capable of facilitating the water oxidation half-reaction and that the primary electron source for CO_2 reduction is the oxidation of furfuryl alcohol. Moreover, recycling experiments presented in Fig. S23 reveal that the CoTPP@CdS-CD retains 81% of its HCOOH evolution activity after three consecutive cycles, illustrating its commendable stability throughout the photocatalytic redox process.

To delve deeper into *β*-CD's influence on CdS-CD, amantadine hydrochloride (AD), known for its robust binding with *β*-CD ($K_S \approx 5.38 \times 10^3$ L mol^{-1}) [51], was introduced as a competitive guest in the CoTPP@CdS-CD photocatalytic system. As presented in Table 1 (entry 6), the introduction of AD considerably reduced HCOOH and furfural yields. This suggests that AD's competition hampered the entry of CoTPP/furfuryl alcohol into the *β*-CD cavity, undermining the photoredox efficiency. This AD and furfuryl alcohol rivalry was further confirmed by ^{1}H NMR measurements (Fig. S24). Subsequent control tests revealed markedly decreased HCOOH and furfural yields in the absence of CoTPP, underscoring the molecular catalyst's pivotal role (Table 1, entry 7). An isotope-labeled ^{13}C NMR experiment utilizing $^{13}CO_2$ displayed a clear H^{13}COOH signal (Fig. S25), supporting the notion that HCOOH primarily arises from CO_2 reduction, rather than organic component degradation [52]. To evaluate the adaptability of the CoTPP@CdS-CD assembly with diverse reactants, we substituted furfuryl alcohol with cinnamic alcohol. As evidenced in Eq. (1) and Fig. S26, using cinnamic alcohol also led to an efficient CO_2 to HCOOH reduction, yielding 1428.3 μmol g^{-1} h^{-1}, comparable to the result with furfuryl alcohol (1609.9 μmol g^{-1} h^{-1}). Notably, cinnamaldehyde emerged as the sole oxidation byproduct, underscoring the selective oxidation of the alcohol segmented over the ethenyl section in cinnamic alcohol.

3.4. Electron transfer kinetics.

To elucidate the contribution of bidirectional host-guest interactions to the exemplary performance of the integrated system, we examined the electron transfer processes among the three components, as illustrated in Scheme 1(a), using a series of steady-state and transient fluorescence spectroscopy experiments. As depicted in Fig. S27 and interpreted through Stern-Volmer analysis of the fluorescence quenching experiments [22], the steady-state emission quenching constant for CoTPP relative to CdS-CD was determined to be 4.31×10^{13} L mol^{-1} s^{-1}. Notably, this value surpasses the upper bound typically observed for discrete systems around 10^{10} L mol^{-1} s^{-1}) [35]. When the competitive guest AD was introduced, this quenching constant declined to 1.35×10^{13} L mol^{-1} s^{-1} (Figs. S28 and S29). It is essential to highlight that the inherent quenching of AD toward CdS-CD was dismissed based on a contrast experiment (Fig. S30); this showed that the mere presence of AD did not induce any fluorescence quenching in CdS-CD. In parallel, an emission quenching test involving furfuryl alcohol and CdS-CD yielded a constant value of 1.48×10^{13} L mol^{-1} s^{-1} (Figs. S31 and S32), which markedly exceeds the recognized limit for discrete systems. This constant was further diminished to 6.64×10^{12} L mol^{-1} s^{-1} with the inclusion of AD (Figs. S33 and S34). Cumulatively, these findings attest to the efficiency of leveraging straightforward host-guest interactions to facilitate electron interactions between the CoTPP catalyst and the furfuryl alcohol reactant on the CdS-CD surface.

The time-resolved photoluminescence decay was subsequently investigated to detect the electron interactions between CdS-CD and CoTPP/furfuryl alcohol. As depicted in Fig. 3(c), upon introducing CoTPP and furfuryl alcohol, the emission lifetime of CdS-CD markedly decreased from an initial 3.73 ns to 1.59 and 2.18 ns, respectively. Moreover, with the concurrent addition of both CoTPP and furfuryl alcohol, the fluorescence lifetime further reduced to 0.58 ns. This reduction highlights the rapid electron transfer among these components. Notably, the dynamic quenching constants (k_q') relating CoTPP/furfuryl alcohol to CdS-CD (Table S4, entries 3 and 5) align closely with the magnitudes observed in steady-state measurements. Delving into the data from the time-resolved photoluminescence decay results (Table S4), the electron transfer rate constants (k_t) between CdS-CD to CoTPP and furfuryl alcohol to CdS-CD were determined to be 3.61×10^8 and 1.91×10^8 s^{-1} respectively. It is notable that these values surpass those observed post the addition of the competitive AD guest (Table S4, entries 4 and 6, Fig. S35). In contrast, the CdS-ME, modified using non-cyclic hydroxyl ligands, showed fluorescence quenching constants and electron transfer rates for furfuryl alcohol and CoTPP that were one and two orders of magnitude lower than those of the CdS-CD system (Fig. S36, Table S4, entries 10 and 11), respectively. In summary, the results convincingly demonstrate that the synergistic host–guest interactions between CdS-CD and CoTPP/alcohol effectively bring the catalyst and reactant together on the CdS NCs' surface. This proximity fosters swift and proficient electron transfers, amplifying the CO_2 photoreduction process.

To further validate the transfer of photogenerated electrons from CdS-CD to CoTPP, irradiated *in-situ* XPS measurements were conducted. As depicted in Fig. 3(d) and Figs. S37–S39, when exposed to light, the binding energies of Co 2*p*, N 1*s*, and Cd 3*d* display negative shifts of 0.2, 0.1, and 0.1 eV respectively. This suggests electron accumulation takes place around the Co, N, and Cd atoms upon light irradiation. Conversely, under the same light exposure, the binding energy of S 2*p* shifts positively by 0.1 eV, suggesting a reduced electron density around the S atoms. These observations underscore that the CO_2 reduction to HCOOH predominantly transpires at the Co site within the CoTPP catalyst. Additionally, the photocurrent, photoluminescence (PL) spectrum, and electrochemical impedance spectroscopy (EIS) results in Fig. S40 highlight the beneficial impact of host-guest bonding between CdS-CD and CoTPP on charge separation.

EPR spectroscopy was employed to identify potential in-

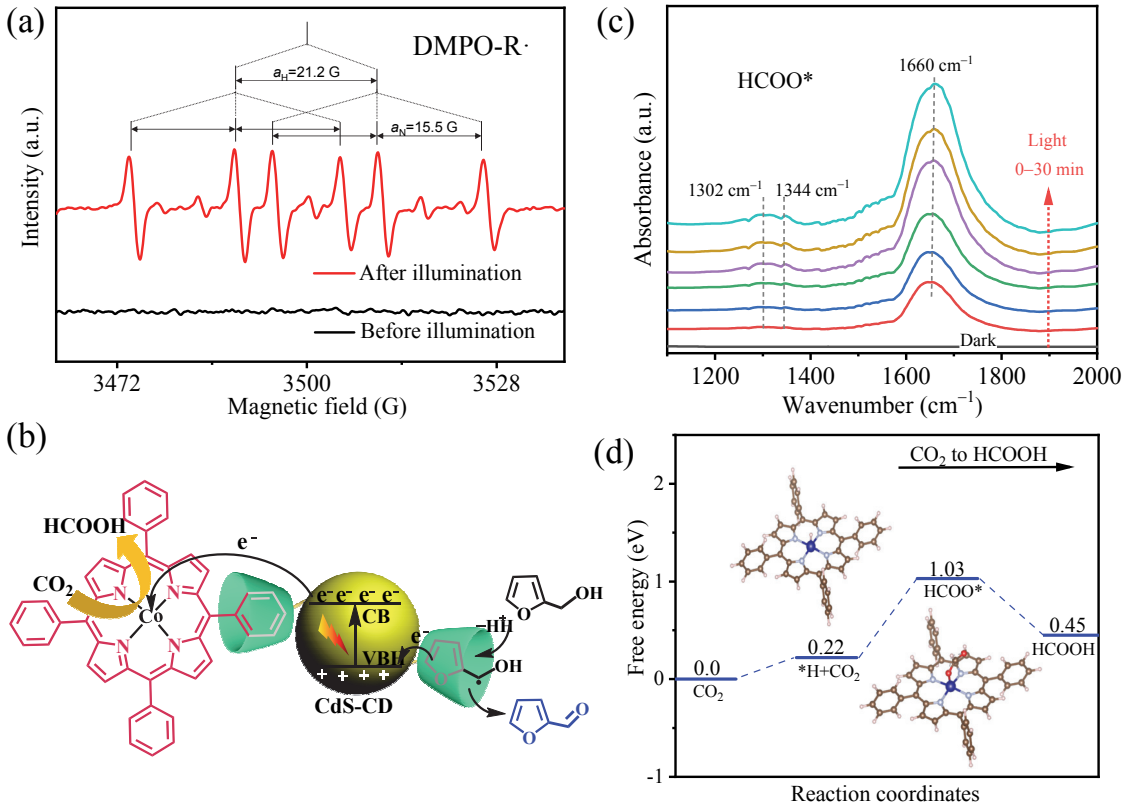

Fig. 4. (a) EPR spectra of the photoreactions under dark and illumination conditions. (b) Proposed mechanism of CoTPP@CdS-CD assembly for CO_2 reduction and furfuryl alcohol oxidation. (c) *In-situ* DRIFT spectra of CO_2 photocatalytic reduction under the atmosphere of CO_2. (d) DFT calculated energy diagram for CO_2 reduction catalyzed by CoTPP. Optimized structures of the intermediates are shown with brown (carbon), pink (hydrogen), red (oxygen), gray (nitrogen), and blue (cobalt).

termediate species during the oxidation of furfuryl alcohol. As depicted in Fig. 4(a), distinctive EPR signals related to the adducts of the alkyl carbon radical and DMPO (5,5-dimethyl-1-pyrroline-*N*-oxide) were detected, with values at a_N = 15.5 G and a_H = 21.2 G. These findings align with previously reported values for the alkyl carbon radical with DMPO (a_N = 15–17 G, a_H = 21–23 G) [20,53], suggesting the formation of furfuryl alcohol benzyl radicals during the photo-induced oxidation reaction. From these results, we proposed a mechanism for the photoredox reaction. As presented in Fig. 4(b), under the irradiation of visible light, CdS-CD generates electrons and holes on its CB and VB, respectively. Given that the onset potential of CoTPP (−0.75 V *vs.* NHE) with CO_2 is less negative than the CB potential of CdS-CD (−0.97 V), the photogenerated electrons on the CB of CdS-CD are readily transferred to the cobalt center of CoTPP. This transfer is facilitated by the host-guest interactions between *β*-CD and the phenyl segment of CoTPP. *In-situ* DRIFT experiments in Fig. 4(c) revealed emerging bands at 1302, 1344, and 1660 cm^{-1} as light exposure increased, suggesting the presence of adsorbed monodentate formate (HCOO*) species on the photocatalyst [54], consistent with the DFT predicted sequence CoTPP-H + CO_2 → CoTPP-HCOO* → CoTPP + HCOOH (Fig. 4(d)). The subsequently formed monoelectronically reduced [Co^{I}TPP]$^-$ species can drive the conversion of CO_2 to HCOOH upon CO_2 binding, following a known mechanism for the photocatalytic conversion of CO_2 to HCOOH [55]. As for the photogenerated holes on the VB of CdS-CD, they possess ample driving force to extract electrons from the furfuryl alcohol molecules housed within the *β*-CD cavities. This action spawns furfuryl alcohol radicals which, after a subsequent oxidation and deprotonation, yield furfural. This reaction pathway underscores the pivotal role of host-guest interactions in enhancing rapid electron/hole transfers and the following redox reactions, achieved by closely aligning the catalyst and reactant on the CdS NCs' surfaces.

4. Conclusions

In conclusion, we devised a straightforward and versatile approach for crafting an effective artificial photosynthesis system. Here, bidirectional host-guest interactions between the photosensitizer and the catalyst/reactant allow for the simultaneous assembly of elements on the photosensitizer's surface. This intimate association shortens the travel distance of photogenerated carriers, significantly enhancing the photocatalytic CO_2 reduction while concurrently oxidizing organics to produce valuable end products. Opting for the simpler oxidation of organics over the more challenging water oxidation reaction not only amplifies the photocatalytic CO_2 reduction but also yields higher-value oxidation products in place of the less desirable

O_2. This makes such systems more practically relevant. Our method stands out against prior covalently linked photosensitizer-catalyst systems. It offers not only simpler construction but also lets the reactant dynamically approach the photosensitizer's surface, facilitating swift intermolecular electron transfer, emulating nature's enzymatic processes. The insights gained here pave the way for constructing high-performing artificial photosynthesis systems for practical applications.

Electronic supporting information

The following files are available free of charge.

Synthesis route of CdS-CD, CdS-OA, CdS-ME, and CdS-BF_4; the determination of CdS Concentration, the Rate of Quenching Constant, Mott-Schottky Plot; the species and selectivity of the products in gas and liquid phase; the characterization of the EPR measurement, IR, NMR, electrochemistry, TEM, XPS, UV-vis spectra and Fluorescence spectra.

Author Contributions

Wen Zhang and Cai-Cai Song contributed equally to this work. Wen Zhang and Tong-Bu Lu conceived and designed the project. Jia-Wei Wang, Shu-Ting Cai, Meng-Yu Gao, and You-Xiang Feng helped with the modification of the paper. Wen Zhang and Tong-Bu Lu wrote and revised the manuscript.

Acknowledgments

We thank Juan Wang for assistance with DFT calculations.

References

[1] C. F. Shih, T. Zhang, J. Li, C. Bai, *Joule*, **2018**, 2, 1925–1949.
[2] L. Wang, W. Chen, D. Zhang, Y. Du, R. Amal, S. Qiao, J. Wu, Z. Yin, *Chem. Soc. Rev.*, **2019**, 48, 5310–5349.
[3] S. Xu, E. A. Carter, *Chem. Rev.*, **2019**, 119, 6631–6669.
[4] X. Li, J. Yu, M. Jaroniec, X. Chen, *Chem. Rev.*, **2019**, 119, 3962–4179.
[5] Y.-B. Chang, C. Zhang, X.-L. Lu, W. Zhang, T.-B. Lu, *Nano Res.*, **2021**, 15, 195–201.
[6] Q. Wang, J. Warnan, S. Rodriguez-Jimenez, J. J. Leung, S. Kalathil, V. Andrei, K. Domen, E. Reisner, *Nat. Energy*, **2020**, 5, 703–710.
[7] Z.-B. Fang, T.-T. Liu, J. Liu, S. Jin, X.-P. Wu, X.-Q. Gong, K. Wang, Q. Yin, T.-F. Liu, R. Cao, H.-C. Zhou, *J. Am. Chem. Soc.*, **2020**, 142, 12515–12523.
[8] S. T. Neaţu, J. A. Macia-Agullo, P. Concepcion, H. Garcia, *J. Am. Chem. Soc.*, **2014**, 136, 15969–15976.
[9] S. Kreft, R. Schoch, J. Schneidewind, J. Rabeah, E. V. Kondratenko, V. A. Kondratenko, H. Junge, M. Bauer, S. Wohlrab, M. Beller, *Chem*, **2019**, 5, 1818–1833.
[10] Z. Jiang, X. H. Xu, Y. H. Ma, H. S. Cho, D. Ding, C. Wang, J. Wu, P. Oleynikov, M. Jia, J. Cheng, Y. Zhou, O. Terasaki, T. Y. Peng, L. Zan, H. X. Deng, *Nature*, **2020**, 586, 549–554.
[11] Y.-F. Xu, M.-Z. Yang, B.-X. Chen, X.-D. Wang, H.-Y. Chen, D.-B. Kuang, C.-Y. Su, *J. Am. Chem. Soc.*, **2017**, 139, 5660–5663.
[12] L.-Y. Wu, Y.-F. Mu, X.-X. Guo, W. Zhang, Z.-M. Zhang, M. Zhang, T.-B. Lu, *Angew. Chem. Int. Ed.*, **2019**, 58, 9491–9495.
[13] L. Yu, X. Ba, M. Qiu, Y. Li, L. Shuai, W. Zhang, Z. Ren, Y. Yu, *Nano Energy*, **2019**, 60, 576–582.
[14] Y. Wang, X. Shang, J. Shen, Z. Zhang, D. Wang, J. Lin, J. C. S. Wu, X. Fu, X. Wang, C. Li, *Nat. Commun.*, **2020**, 11, 3043.
[15] J. Wu, X.-D. Li, W. Shi, P.-Q. Ling, Y.-F. Sun, X. C. Jiao, S. Gao, L. Liang, J.-Q. Xu, W.-S. Yan, C.-M. Wang, Y. Xie, *Angew. Chem. Int. Ed.*, **2018**,

Graphical Abstract

Chin. J. Catal., 2023, 52: 176–186 doi: 10.1016/S1872-2067(23)64509-7

Bidirectional host-guest interactions promote selective photocatalytic CO_2 reduction coupled with alcohol oxidation in aqueous solution

Wen Zhang [a], Cai-Cai Song [a], Jia-Wei Wang [b], Shu-Ting Cai [a], Meng-Yu Gao [a], You-Xiang Feng [a], Tong-Bu Lu [a,*]
Tianjin University of Technology; Sun Yat-sen University

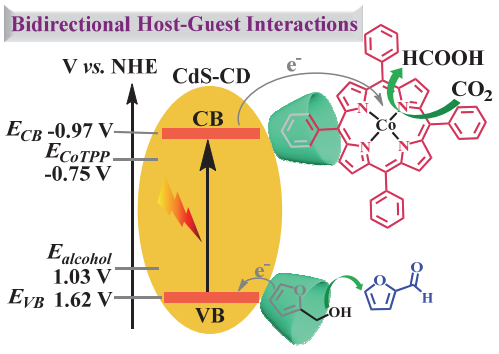

Leveraging bidirectional host-guest interactions, both the Co meso-tetraphenyl porphyrin catalyst and alcohol reactant can be gathered on the surface of mono-(6-mercapto-6-deoxy)-*β*-cyclodextrin-decorated CdS nanocrystals. This arrangement spurs efficient CO_2 reduction coupled with organic oxidation in aqueous solutions by promoting expedited electron/hole extraction from CdS nanocrystals.

57, 8719–8723.
[16] Q.-Q. Bi, J.-W. Wang, J.-X. Lv, J. Wang, W. Zhang, T.-B. Lu, *ACS Catal.*, **2018**, 8, 11815–11821.
[17] T. Ouyang, H.-J. Wang, H.-H. Huang, J.-W. Wang, S. Guo, W.-J. Liu, D.-C. Zhong, T.-B. Lu, *Angew. Chem. Int. Ed.*, **2018**, 57, 16480–16485.
[18] C. Cometto, R. Kuriki, L. Chen, K. Maeda, T.-C. Lau, O. Ishitani, M. Robert, *J. Am. Chem. Soc.*, **2018**, 140, 7437–7440.
[19] Y.-X. Feng, H.-J. Wang, J.-W. Wang, W. Zhang, M. Zhang, T.-B. Lu, *ACS Appl. Mater. Interfaces*, **2021**, 13, 26573–26580.
[20] Q. Guo, F. Liang, X.-B. Li, Y.-J. Gao, M.-Y. Huang, Y. Wang, S.-G. Xia, X.-Y. Gao, Q.-C. Gan, Z.-S. Lin, C.-H. Tung, L.-Z. Wu, *Chem*, **2019**, 5, 2605–2616.
[21] V. S. Thoi, N. Kornienko, C. G. Margarit, P. Yang, C. J. Chang, *J. Am. Chem. Soc.* **2013**, 135, 14413–14424.
[22] J.-W. Wang, L. Jiang, H.-H. Huang, Z. Han, G. Ouyang, *Nat. Commun.*, **2021**, 12, 4276.
[23] D. Hong, Y. Tsukakoshi, H. Kotani, T. Ishizuka, T. Kojima, *J. Am. Chem. Soc.*, **2017**, 139, 6538–6541.
[24] L. Yuan, M.-Y. Qi, Z.-R. Tang, Y.-J. Xu, *Angew. Chem. Int. Ed.*, **2021**, 60, 21150–21172.
[25] E. Lam, E. Reisner, *Angew. Chem., Int. Ed.*, **2021**, 60, 23306–23312.
[26] Y. L. Wu, M. Y. Qi, C. L. Tan, Z. R. Tang, Y. J. Xu, *Chin. J. Catal.*, **2022**, 43, 1851−1859.
[27] Y. H. Li, Z. R. Tang, Y. J. Xu, *Chin. J. Catal.*, **2022**, 43, 708–730.
[28] J. Y. Li, M. Y. Qi, Y. J. Xu, *Chin. J. Catal.*, **2022**, 43, 1084–1091.
[29] M. Y. Qi, M. Conte, Z. R. Tang, Y. J. Xu, *ACS Nano*, **2022**, 16, 17444–17453.
[30] M. Y. Qi, M. Conte, M. Anpo, Z. R. Tang, Y. J. Xu, *Chem. Rev.*, **2021**, 121, 13051–13085.
[31] A. V. Puga, *Coord. Chem. Rev.*, **2016**, 315, 1–66.
[32] K. Wu, Y. Du, H. Tang, Z. Chen, T. Lian, *J. Am. Chem. Soc.*, **2015**, 137, 10224–10230.
[33] M. J. Berr, P. Wagner, S. Fischbach, A. Vaneski, J. Schneider, A. S. Susha, A. L. Rogach, F. Jäckel, J. Feldmann, *Appl. Phys. Lett.*, **2012**, 100, 223903.
[34] J. Yang, D. Wang, H. Han, C. Li, *Acc. Chem. Res.*, **2013**, 46, 1900–1909.
[35] K. E. Knowles, M. Malicki, E. A. Weiss, *J. Am. Chem. Soc.*, **2012**, 134, 12470–12473.
[36] F. Li, Y. Jiang, B. Zhang, F. Huang, Y. Gao, L. Sun, *Angew. Chem. Int. Ed.*, **2012**, 51, 2417–2420.
[37] K. Koike, D. C. Grills, Y. Tamaki, E. Fujita, K. Okubo, Y. Yamazaki, M. Saigo, T. Mukuta, K. Onda, O. Ishitani, *Chem. Sci.*, **2018**, 9, 2961–2974.
[38] Y. Tamaki, O. Ishitani, *ACS Catal.*, **2017**, 7, 3394–3409.
[39] M. F. Kuehnel, K. L. Orchard, K. E. Dalle, E. Reisner, *J. Am. Chem. Soc.*, **2017**, 139, 7217–7223.
[40] S. Lian, M. S. Kodaimati, E. A. Weiss, *ACS Nano*, **2018**, 12, 568–575.
[41] P. L. Cheung, S. C. Kapper, T. Zeng, M. E. Thompson, C. P. Kubiak, *J. Am. Chem. Soc.*, **2019**, 141, 14961–14965.
[42] R. Kuriki, M. Yamamoto, K. Higuchi, Y. Yamamoto, M. Akatsuka, D. Lu, S. Yagi, T. Yoshida, O. Ishitani, K. Maeda, *Angew. Chem. Int. Ed.*, **2017**, 56, 4867–4871.
[43] X.-M. Hu, M. H. Rønne, S. U. Pedersen, T. Skrydstrup, K. Daasbjerg, *Angew. Chem. Int. Ed.*, **2017**, 56, 6468–6472.
[44] J. Shen, M. J. Kolb, A. J. Göttle, M. T. M. Koper, *J. Phys. Chem. C*, **2016**, 120, 15714–15721.
[45] J. Wang, Y.-X. Feng, M. Zhang, C. Zhang, M. Li, S.-J. Li, W. Zhang, T.-B. Lu, *CCS Chem.*, **2020**, 2, 81–88.
[46] L. Chen, Y. Chen, Y. Zhang, Y. Liu, *Angew. Chem. Int. Ed.*, **2021**, 60, 7654–7658.
[47] Y. Qiu and A. E. Kaifer, *Isr. J. Chem.*, **2011**, 51, 830–839.
[48] Y.-M. Zhang, Y.-H. Liu and Y. Liu, *Adv. Mater.*, **2020**, 32, 1806158.
[49] Z.-Q. Li, Y.-M. Zhang, H.-Z. Chen, J. Zhao, Y. Liu, *J. Org. Chem.*, **2013**, 78, 5110–5114.
[50] C.-M. Chang, K.-L. Orchard, B. C. M. Martindale, E. Reisner, *J. Mater. Chem. A*, **2016**, 4, 2856–2862.
[51] F.-F. Shen, Y.-M. Zhang, X.-Y. Dai, H.-Y. Zhang, Y. Liu, *J. Org. Chem.*, **2020**, 85, 6131–6136.
[52] G.-X. Dong, W. Zhang, Y.-F. Mu, K. Su, M. Zhang, T.-B. Lu, *Chem. Commun.*, **2020**, 56, 4664–4667.
[53] G. R. Buettner, *Free Radical Biol. Med.*, **1987**, 3, 259–303.
[54] A. Haghofer, D. Ferri, K. Föttinger, and G. Rupprechter. *ACS Catal.*, **2012**, 2, 2305–2315.
[55] A. J. Morris, G. J. Meyer, E. Fujita, *Acc. Chem. Res.*, **2009**, 42, 1983–1994.

双向主客体作用促进水溶液中选择性光催化CO_2还原与醇氧化

张　雯[a,1], 宋彩彩[a,1], 王嘉蔚[b], 蔡舒婷[a], 高梦语[a], 冯有祥[a], 鲁统部[a,*]
[a]天津理工大学化学与化工学院, 有机太阳能电池与光化学转化天津重点实验室, 材料科学与工程学院, 新能源材料与低碳技术研究院, 材料微结构教育部国际合作联合实验室, 天津300384
[b]中山大学化学学院, 环境与能源化学系KLGHEI, 广东广州510275

摘要: CO_2还原与H_2O氧化耦合被认为是将太阳能转化为化学能的理想方法. 然而, H_2O氧化反应的显著动力学障碍限制了该类反应的转化效率. 此外, 额外的电子牺牲剂的消耗不仅在经济上不可行, 而且浪费了光生空穴的氧化能力. 因此, 将CO_2还原与有机物的有效氧化相结合将是有效利用太阳能和解决能源危机的有效途径之一. 对于包含光敏剂、催化剂和反应底物的离散光催化体系来说, 电子转移效率主要由离散组分之间的扩散过程控制. 为了提高光反应组分之间的电子转移效率, 研究人员尝试通过共价键在催化剂和光敏剂之间建立“桥梁”, 从而获得更快的电子转移速率. 然而, 该类体系存在合成过程复杂、共价键断裂及使用贵金属等问题. 与共价键相比, 非共价体系更便于合成, 且具有更好的稳定性.

本文利用双向主客体相互作用构筑高效光催化体系, 其中水溶性*β*-环糊精修饰的CdS纳米晶与CoTPP(助催化剂)和有机醇(反应底物)均通过非共价主客体作用连接, 促使光生电子和光生空穴的同步快速消耗. 核磁共振氢谱结果表明, 环糊精作为主体分子可以识别客体分子四苯基卟啉钴与呋喃醇. 利用Job曲线测得环糊精与四苯基卟啉钴以及呋喃醇的键合比分别为2:1和1:1. 紫外-可见吸收光谱结果表明, 环糊精与四苯基卟啉钴以及呋喃醇之间存在不同强度的主客体键合. 光催

化CO_2还原反应与呋喃醇氧化性能测试结果表明, 与无配体的CdS纳米晶(CdS-BF_4)以及其它配体(油酸、2-巯基乙醇和硫代甘油)修饰的CdS纳米晶相比, 环糊精修饰的CdS-CD纳米晶在水相中表现出更高的CO_2还原为HCOOH的活性与选择性, 同时, 表现出最佳的呋喃醇氧化活性与选择性. 相反, 表面无配体的CdS-BF4纳米晶活性较低, 且有严重的析氢副反应发生. 为了更好地理解双向主客体相互作用对光反应性能的贡献, 利用一系列稳态和瞬态荧光光谱实验研究了三个组分之间的电子转移过程. 结果表明, CdS-CD与CoTPP之间以及CdS-CD与呋喃醇之间的双向主客体相互作用可以有效促进这些组分之间的电子转移过程. 原位漫反射傅立叶变换红外光谱和密度泛函理论研究表明, 随着光辐射时间的增加, HCOO*信号逐渐增强. 电子顺磁共振波谱结果表明, 在光催化呋喃醇氧化的过程中产生了呋喃醇苄基自由基. 在以上光还原和光氧化的全反应过程中, 双向主客体作用同时将助催化剂和反应物聚集在吸光物质CdS NCs表面, 这对于促进快速电子/空穴转移和随后的氧化还原反应发挥着关键作用.

综上所述, 选择合适的有机物不仅可以促进光还原反应的发生, 还可以生产更高附加值的化学品. 本文采用双向主客体策略构建新型的人工光合作用系统, 为构建具有实际应用潜能的人工光合作用系统提供了新的思路.

关键词: 人工光合成; 主客体相互作用; CO_2还原; 醇氧化; 快速电子转移

收稿日期: 2023-05-17. 接受日期: 2023-08-13. 上网时间: 2023-09-25.

*通讯联系人. 电子信箱: lutongbu@tjut.edu.cn (鲁统部).

[1]共同第一作者.

基金来源: 国家自然科学基金(21702146, 21790052, 21931007); 国家重点研发计划项目(2017YFA0700104); 国家111项目(D17003); 天津市自然科学基金资助项目(19JCQNJC05500).